NANO · MICRO small
www.small-journal.com

Overcoming the Interfacial Limitations Imposed by the Solid–Solid Interface in Solid-State Batteries Using Ionic Liquid-Based Interlayers

Syed Atif Pervez, Guktae Kim, Bhaghavathi P. Vinayan, Musa A. Cambaz, Matthias Kuenzel, Maral Hekmatfar, Maximilian Fichtner, and Stefano Passerini**

Li-garnets are promising inorganic ceramic solid electrolytes for lithium metal batteries, showing good electrochemical stability with Li anode. However, their brittle and stiff nature restricts their intimate contact with both the electrodes, hence presenting high interfacial resistance to the ionic mobility. To address this issue, a strategy employing ionic liquid electrolyte (ILE) thin interlayers at the electrodes/electrolyte interfaces is adopted, which helps overcome the barrier for ion transport. The chemically stable ILE improves the electrodes-solid electrolyte contact, significantly reducing the interfacial resistance at both the positive and negative electrodes interfaces. This results in the more homogeneous deposition of metallic lithium at the negative electrode, suppressing the dendrite growth across the solid electrolyte even at high current densities of 0.3 mA cm^{-2}. Further, the improved interface Li/electrolyte interface results in decreasing the overpotential of symmetric Li/Li cells from 1.35 to 0.35 V. The ILE modified Li/LLZO/LFP cells stacked either in monopolar or bipolar configurations show excellent electrochemical performance. In particular, the bipolar cell operates at a high voltage (≈8 V) and delivers specific capacity as high as 145 mAh g^{-1} with a coulombic efficiency greater than 99%.

1. Introduction

Li-ion batteries (LIBs) are the linchpin of the electric vehicles (EVs) industry and are therefore the focus of continued innovation.[1–3] In a quest to overcome the limitations of LIBs such as their lower safety and energy density, solid state batteries (SSBs) have emerged as potential game changers for the EV application.[4–6] SSBs employ solid electrolytes (SEs) that offer several advantages over their liquid counterparts such as wider electrochemical stability (operative potential) window, non-flammability, and higher ionic transference numbers.[7–9] Inorganic type SEs have demonstrated high room temperature ionic conductivities (≈10^{-3} S cm^{-1}) and good mechanical strength. However, device integration of such SEs is far from successful either due to parasitic chemical/electrochemical reactions that may take place at the electrode-electrolyte interface or poor mechanical contacts due to the solid-solid nature of the interface. Among various types of inorganic SEs, lithium lanthanium zirconate (LLZO) is an interesting choice due to its thermodynamic stability in a rather wide potential window.[4,10] In comparison to other solid-electrolytes, density functional theory studies suggest that LLZO is electrochemically more stable with Li metal and high voltage metal-oxide cathodes ($LiCoO_2$, $LiNi_{0.5}Mn_{1.5}O_4$, and $LiFePO_4$).[11]

However, despite having good electrochemical stability, LLZO SEs are stiff and brittle in nature, that restricts their intimate physical contact with both the Li and the positive electrodes thus resulting in high interface resistance[12] and poor utilization of electrode active materials. Furthermore, such uneven Li/SE contacts play a major role in initiating Li dendrites at the interfaces.[13,14] Various strategies have been adopted to provide and maintain an intimate contact between Li and LLZO, for example, coating of the SE surface with metal or metal-oxide nano-layers such as Al_2O_3,[12] Au,[13] Al,[15] Ge,[16] and ZnO[17]. On the cathode side, 3D designing of the LLZO surface, sputtering and/or melting cathode materials on the SE surface have been demonstrated as effective strategies.[18–20] These works, however, adopt vacuum-based techniques or high temperature steps which may affect the scalability of the synthesis process and increase the cost.

Dr. S. A. Pervez, Dr. G. Kim, Dr. B. P. Vinayan, M. A. Cambaz, Dr. M. Kuenzel, Dr. M. Hekmatfar, Prof. M. Fichtner, Prof. S. Passerini
Helmholtz Institute Ulm
Helmholtzstraße, 11, D-89081 Ulm, Germany
Dr. S. A. Pervez, Dr. G. Kim, Dr. B. P. Vinayan, M. A. Cambaz, Dr. M. Kuenzel, Dr. M. Hekmatfar, Prof. S. Passerini
Karlsruhe Institute of Technology
P.O. Box 3640, D-76021 Karlsruhe, Germany
E-mail: stefano.passerini@kit.edu
Prof. M. Fichtner
Karlsruhe Institute of Technology
Institute of Nanotechnology
P.O. Box 3640, D-76021 Karlsruhe, Germany
E-mail: maximilian.fichtner@kit.edu
The ORCID identification number(s) for the author(s) of this article can be found under https://doi.org/10.1002/smll.202000279.

DOI: 10.1002/smll.202000279

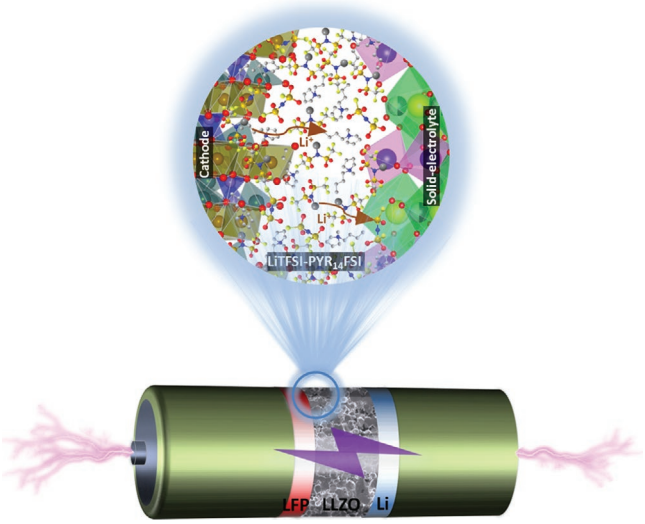

Figure 1. Schematic illustration of the interface between LLZO SE and LFP cathode. "magnified view" shows the ILE interlayer between the cathode and the solid electrolyte enabling fast ionic transport.

An interesting approach to tackle the issue of high interface resistance is to introduce ion conducting polymeric layers, gels and/or liquids as wetting agents at the interfaces.[21–25] In such designs, the Li ion conducting polymer or liquid fills the voids at the interface that ensures intimate electrode–electrolyte contact while the SE acts as a separator as well as single ion transfer medium ($t_{Li^+} \approx 1$). Use of liquid ion conductors may prove more efficient, especially on the cathode side since liquids can penetrate through the pores of the composite electrode hence accessing a greater cathode surface area and providing interfacial paths for ionic transport at the interfaces.

Room temperature ILEs represent potential alternatives to the conventional carbonate-based liquid electrolytes thanks to their much improved thermal stability, extremely low flammability, and wider potential window.[26,27] Such features make them highly compatible with LLZO since the latter also offer similar properties. Herein, we report an interface modification strategy where ILE interlayers are introduced at the electrodes-LLZO interfaces to improve interfacial properties of LLZO SE based SSB. In the proposed design the ILE acts as medium for Li ions transport by filling the voids at the electrodes-LLZO junctions as schematically shown in **Figure 1**. Mixture of *N*-butyl-*N*-methyl-pyrrolidinium bis(fluorosulfonyl)imide ($Pyr_{14}FSI$) and lithium bis(trifluoromethane-sulfonyl)imide (LiTFSI) salts (see Figure S1, Supporting Information) is chosen as the ILE due to its additional benefits over other types of IL-electrolytes, that is, lower viscosity, and better electrochemical stability with the Li anode.[28] Results show a good chemical stability of the ILE with LLZO SE. Further, with ILE-interlayers at the Li/SE and LFP/SE interfaces the interfacial resistances are drastically reduced resulting in suppression of Li dendrites and stabilized electrochemical performance.

2. Results and Discussions

In this work, niobium- (Nb) and barium- (Ba) doped Li-garnet ($Li_{6.5}La_{2.5}Ba_{0.5}ZrNbO_{12}$) is used. The supervalent cation (Nb^{5+}) doping at the Zr^{4+} sites creates Li^+ vacancies and stabilizes the cubic phase.[29] Further, partial substitution of low-valent alkaline-earth metal cations (Ba^{2+}) at the La^{3+} site increases Li^+ concentration in the LLZO framework.[30] Both ways of doping eventually result in improved Li^+ conductivity in the LLZO SE. **Figure 2**a shows the cross-sectional scanning electron microscopy (SEM) image of the LLZO SE pelletized using a uniaxial press and then sintered via two-step process (at 900 °C for 24 h and then at 1100 °C for 3 h) in alumina crucibles. A photo of the sintered LLZO pellet is shown in the inset of Figure 2a while a low magnification SEM image is shown in Figure S2, Supporting Information. The sintering and pellet pressing conditions were optimized to get the pure cubic phase and high relative density. The cubic phase has been preferred over tetragonal phase of LLZO because of its higher ionic conductivity[4] while the high density of the pellet helps in restricting Li dendrite growth across the grain boundaries and pores of the SE.[31] As evident from the SEM cross-sectional image (Figure 2a), the LLZO pellet is densely packed with grain size in μm range. EDS mapping and spectra of the LLZO SE are shown in Figure S3, Supporting Information. From the elemental mapping no significant segregation of the core elements (La, Ba, Nb, Zr, O) is observed. Also, the Al contamination from the alumina crucible seems to be well distributed along the cross-section of the SE. The Al incorporation helps in stabilizing the structure in the highly conducting cubic phase, and suppresses the formation of the pyrochlore-type $La_2Zr_2O_7$ impurity phases which are known for degrading the ionic conductivity of LLZO.[32,33] The X-ray diffraction (XRD) patterns for the sintered LLZO SE (Figure 2b) confirm the formation of the cubic phase LLZO. Most of the diffraction peaks are indexed to the parent Li-garnet phase "$Li_5La_3Nb_2O_{12}$" (JCPDS # 00-045-0109) with the space group *Ia-3d*.[4,34] Room temperature (25 °C) Nyquist impedance plots for Au/LLZO/Au symmetrical cells with equivalent circuit diagram are shown in Figure 2c. The high frequency ($f \approx 1$ MHz, $C \approx 10^{-10}$ F) semicircle corresponds to the inter-grain (bulk) and intra-grain (grain-boundary) impedances of the SE, while the low frequency ($f \approx 50$ Hz, $C \approx 10^{-7}$ F) tail corresponds to the interface impedance.[35] Since Au electrodes are quasi-blocking toward Li^+ ion diffusion at the interface, very large impedance is observed in the form of a steep, but still sloping line. The impedance data was fitted with a suitable equivalent circuit using *R*, representing resistance of the SE, and constant phase element (CPE) representing non-ideal capacitance taking into account the depressed semi-circles. The total, bulk, and grain boundary resistance (R_{B+GB}) derived from the low frequency intercept of the semi-circle with the *Z' axis* is ≈ 520 Ω cm^{-2}. This value is used to calculate the ionic conductivity of the SE using the formula: $\sigma = t\ (R_{B+GB}\ a)^{-1} \approx 10^{-4}$ S cm^{-1}, where "*t*" is the thickness and "*a*" is the geometric area of the SE pellet. The impedance measurements were repeated at higher temperatures (up to 100 °C) to calculate the value of '*σ*'. Since Li^+ ion conduction in LLZO is thermally activated, the SE resistance decreases with increasing temperatures. The conductivity versus temperature plot (Figure 2d), follows the typical Arrhenius behavior, which can be expressed as follows

$$\sigma = \left(\frac{A}{T}\right)\exp\left(\frac{-E_a}{kT}\right) \quad (1)$$

where "*A*" is the frequency factor, "*T*" the temperature in Kelvin, "E_a" the activation energy expressed in J $mole^{-1}$, and "*k*" is Boltzmann's constant. Note that the "*σ*" data obtained at

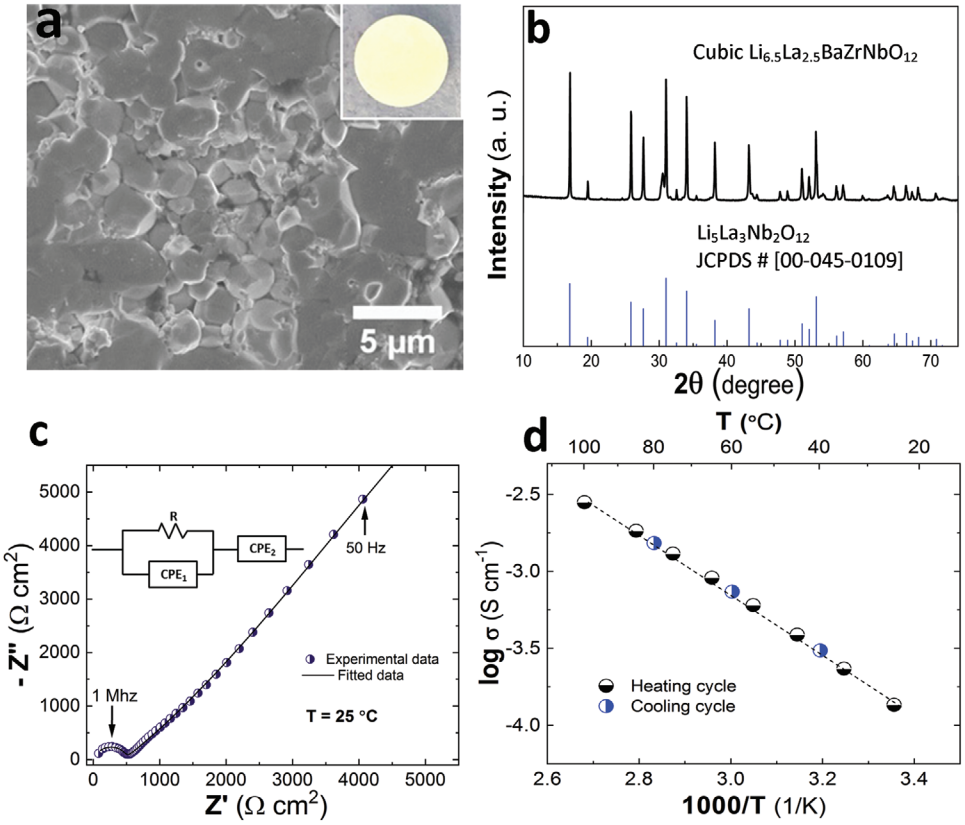

Figure 2. a) Cross-sectional SEM image of LLZO. The inset shows an optical image of the LLZO pellet. b) X-ray diffraction patterns of $Li_{6.5}La_{2.5}Ba_{0.5}ZrNbO_{12}$ and calculated pattern for cubic garnet ($Li_5La_3Nb_2O_{12}$, JCPDS # 00-045-0109). c) AC impedance spectra of Au/LLZO/Au cell at room temperature. Inset shows the equivalent circuit used to fit the impedance data. d) Arrhenius plot of LLZO conductivity.

different temperatures follow the same line during heating and cooling cycles suggesting thermal equilibrium and stability of the LLZO SE.

For a stable interface the chemical compatibility of the ILE with LLZO is of utmost importance. To check this, LLZO pellets were immersed in the ILE (0.2LiTFSI – 0.8Pyr_{14}FSI) for one week. Prior to characterization by XRD and Raman spectroscopy, the pellets were thoroughly washed with 2-propanol to get rid of any residual ILE left on the surface. From naked eye observation, there was no apparent change in the color of the LLZO pellet after exposure to the ILE as shown in Figure S4, Supporting Information. Comparing the XRD patterns of LLZO pellets before and after exposure to the ILE (**Figure 3**a) it is seen that all major diffraction peaks for the cubic LLZO phase are present while no new diffraction peaks appear, suggesting for the chemical stability of LLZO in contact with the ILE. Further, the ILE-exposed surface of LLZO was analyzed by Raman spectroscopy. The Raman spectra for both the samples consist of typical LLZO energy bands at < 300, 300–550, and >550 cm^{-1} assigned to the La cation vibrations, Li—O bond stretching and Zr—O vibrational stretching modes, respectively.[36,37] The comparison of the spectra obtained for LLZO SEs before and after exposure to IL reveals no shift in the LLZO energy bands except a small peak at ≈1090 cm^{-1} which suggests the presence of carbonate layers on the surface (Figure 3b). These layers, with thickness in the nanometer range, start to form when LLZO is exposed to ambient air.[36,38] To confirm that the carbonate layers are limited only to the surface, Raman spectra were taken upon depth profiling. As evident from the spectra and the Raman mapping (for the band at 1090 cm^{-1}, Figure S5, Supporting Information), the sub-surface of the ILE exposed LLZO pellet is free from carbonates species. The absence of any other compounds on the pellet's surface is also supporting a chemical stability of the ILE versus LLZO.

EIS investigation was carried out for three different types of symmetrical cells: Li/LLZO/Li without and with ILE interlayers, and LFP/LLZO/LFP with ILE interlayers. All measurements were performed at room temperature (25 °C). The Nyquist plots (**Figure 4**) consist of two depressed semicircles in the high and low frequency regions. The semicircle at high frequency corresponds to the bulk and grain-boundary impedance of the LLZO SE, whereas that at lower frequencies relates to the interface charge transfer.[35] For each cell the total SE resistance (R_{B+GB}) is evaluated fitting the high frequency semicircle for each cell (Figure 4 and inset). The obtained values are listed in **Table 1**. For Au/LLZO/Au symmetric cell R_T is ≈ 520 Ω cm^2 (derived from Nyquist plots in Figure 2c), which is the bulk resistance (inter-grain and intra-grain resistances) of the SE. This value excludes interface resistance since no (or negligibly small) Li ion transport will occur due to the quasi-blocking nature of Au electrodes towards Li ions. However, with Li or LFP electrodes replacing Au, Li ions can transfer across the interface and, thus, the interfacial resistance is observed. This is the origin of the

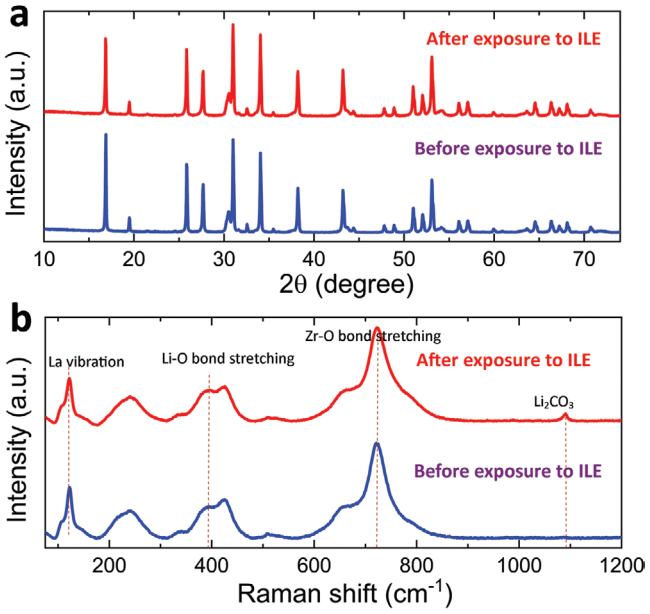

Figure 3. Chemical stability of $Li_{6.5}La_{2.5}Ba_{0.5}ZrNbO_{12}$ SE and 0.2LiTFSI-0.8Pyr_{14}FSI ionic liquid a) X-ray diffraction patterns before and after soaking in ionic liquid for one week. b) Raman spectra before and after soaking in ionic liquid for one week.

second semicircle that corresponds to the interfacial resistance, R_I. The Li/LLZO/Li symmetric cell without ILE displays a relatively high charge transfer resistance (≈4900 Ω cm^2), while the Li/LLZO/Li and LFP/LLZO/LFP cells employing the ILE interlayers display only ≈290 Ω cm^2 and ≈530 Ω cm^2, respectively. Since the cells are symmetric, the value of R_I for an individual interface is calculated by dividing the overall charge transfer resistance by a factor of 2. Comparing the values (Table 1), the cells employing the ILE interlayers show significantly lower interfacial resistances, R_I for Li/LLZO/Li reduces to ≈145 Ω cm^2 while for LFP/LLZO/LFP to ≈265 Ω cm^2, than the one without ILE. It is important to mention that the ILE itself imparts a very

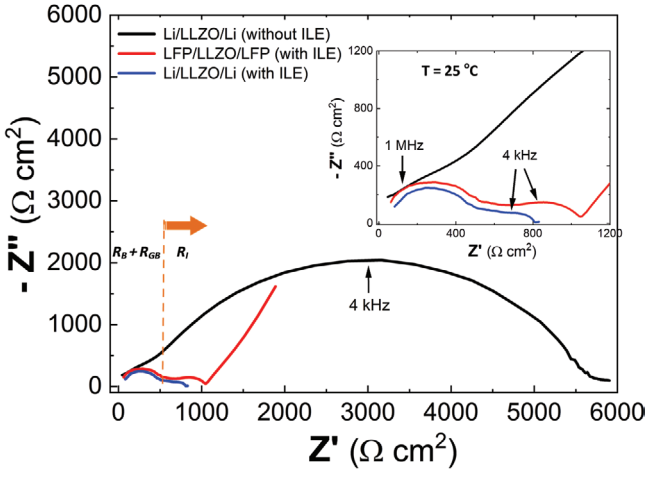

Figure 4. AC impedance plots for symmetric cells: Li/LLZO/Li without and with ILE, and LFP/LLZO/LFP with ILE cells. The inset shows a magnification of the high frequency part of the plots. All measurements were performed at 25 °C.

Table 1. Bulk and interface resistance values for the different cells. The values are extracted from the AC impedance plots.

Sample	*RT* [ca Ω cm^2]	*RI* [ca Ω cm^2]
Au/LLZO/Au	520	—
Li/LLZO/Li(without ILE)	520	2440
Li/LLZO/Li(with ILE)	520	145
LFP/LLZO/LFP(with ILE)	520	265
SS/ILE/SS	9	—

small contribution to the electrolyte resistance (≈ 9 Ω cm^2 at each interface) as evaluated from the Nyquist plot in Figure S6, Supporting Information. The ionic conductivity of the ILE is ≈3 × 10^{-4} S cm^{-1} at room temperature. These results clearly indicate a favorable role of the ILE in reducing the interfacial resistances both at the Li anode and at the LFP cathode interfaces with LLZO.

The Li stripping/plating voltage profiles for symmetrical Li/LLZO/Li cells with and without the ILE interlayers are compared in **Figure 5**. While the cell with the ILE was tested at 0.2 mA cm^{-2} (Li charge capacity: 0.05 mAh cm^{-2} per cycle) and 0.3 mA cm^{-2} (Li charge capacity: 0.075 mAh cm^{-2} per cycle) the one without ILE was tested at 0.1 mA cm^{-2} (Li charge capacity: 0.025 mAh cm^{-2} per cycle) and 0.2 mA cm^{-2} (Li charge capacity: 0.05 mAh cm^{-2} per cycle) due to the much higher overpotential. As shown in Figure 5a, Li/LLZO/Li with ILE shows a stable and reversible Li stripping/plating voltage response at the chosen current densities for more than 120 h, after which the experiment was terminated in the absence of anomalous events. The "magnified view" of the voltage profiles in Figure 5b clearly shows that the voltage polarizations are reasonably stable even after more than 100 h of continuous Li stripping and plating. On the contrary, the response of the Li/LLZO/Li symmetric cell without IL is not satisfactory. At relatively low current density (0.1 mA cm^{-2}) the voltage profiles are somewhat stable; however, by switching to higher current density (0.2 mA cm^{-2}), random oscillations and fluctuations starts to appear (Figure 5c,d). Also, the overpotential is significantly higher (≈1.35 V at 0.2 mA cm^{-2}) when compared to Li/LLZO/Li with ILE (≈0.35 V at 0.2 mA cm^{-2}). The fluctuations in the voltage profiles indicate uneven Li stripping that decrease sites for Li transfer and change the actual Li/LLZO contact area. Such an unstable interface may also provide nucleation sites for Li-dendrites growth. Note that with the ILE interlayers at the interface, Li/LLZO/Li cells do not show such irregular voltage profiles even at higher current densities and longer duration of cycling, indicating that the ILE is very effective in enabling higher stripping/plating currents while preventing the dendritic growth of lithium. To further support this evidence, the average voltage hysteresis was measured for both cells and the values are plotted vs. cycle number as shown in Figure S7, Supporting Information. The voltage hysteresis is the difference between the stripping and the plating voltages and is mainly determined by the magnitude of applied current and the overall cell resistance, including that arising from the interfaces.[39,40] As expected Li/LLZO/Li without the ILE demonstrated irregular and fluctuating voltage hysteresis at 0.2 mA cm^{-2}, which indicates for the instability of Li–SE

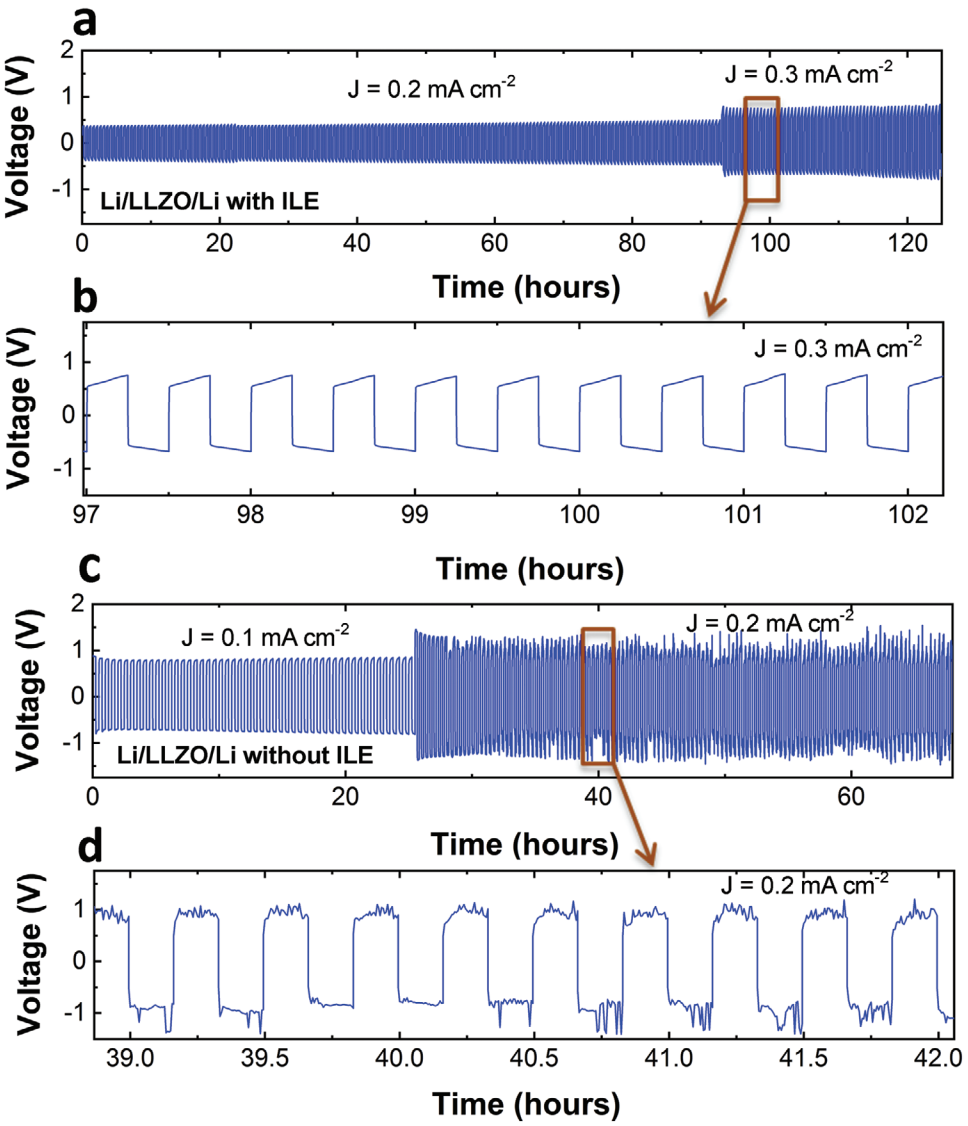

Figure 5. Li stripping/plating voltage profiles of symmetric Li/LLZO/Li cells a,b) with and c,d) without ILE. The tests were conducted at 25 °C.

interface. On the contrary, Li/LLZO/Li with the ILE interlayer shows a stable voltage hysteresis even though the cells were cycled at higher current density (0.3 mA cm^{-2}). The poor contact between the Li and the LLZO will give rise to localized current flowing in the limited positions where Li is interfaced with the SE. Such spots will then act as favorable sites for Li dendrite initiation and growth during subsequent Li cycling. In this context the role of ILE is very important in homogenizing the Li flux through the interface, resulting in the suppression of Li dendritic growth as it was also demonstrated adopting other interface modification techniques.[13,22,41]

To check the suitability of the proposed electrolytes, Li/LLZO/LFP cells were subjected to galvanostatic cycling at current densities ranging from 20 to 100 mA $g_{(LFP)}^{-1}$ (**Figure 6**). Nano sized LFP powders (particle size ≈ 100 nm) were used as the cathodes. The LFP powders were carbon-coated to improve their conductivity. The morphology of the particles was not affected by the coating as shown in SEM images in Figure S8, Supporting Information. A few µLs of ILE were deposited onto the Li and the LFP electrode surfaces facing the SE. Figure 6a shows the first and fifth galvanostatic charge/discharge voltage profiles at current density of 20 mA $g_{(LFP)}^{-1}$ in the 2.8–4.0 V voltage window at 25 °C. The cells show a reversible capacity of ≈145 mAh $g_{(LFP)}^{-1}$ with a coulombic efficiency of ≈99.9%. The typical flat voltage profiles with a very low polarization indicative of the reversible insertion of Li^+ in the LFP olivine structure.[42,43] This was further confirmed by the cyclic voltammetry test as shown in Figure S9, Supporting Information. Well defined redox peaks in the range of 3–4 V are observed that are attributed to the Fe^{2+}/Fe^{3+} redox couple reaction, corresponding to lithium (de-) insertion in the LFP olivine crystal structure. The cell was also tested at elevated current densities to check its rate performance. At 40, 60, 80, and 100 mA $g_{(LFP)}^{-1}$ the cell delivers discharge capacities of ≈136, 125, 117, and 112 mAh g^{-1}, respectively. Switching back to 20 mA $g_{(LFP)}^{-1}$, the initial capacity (≈145 mAh $g_{(LFP)}^{-1}$) is fully recovered and

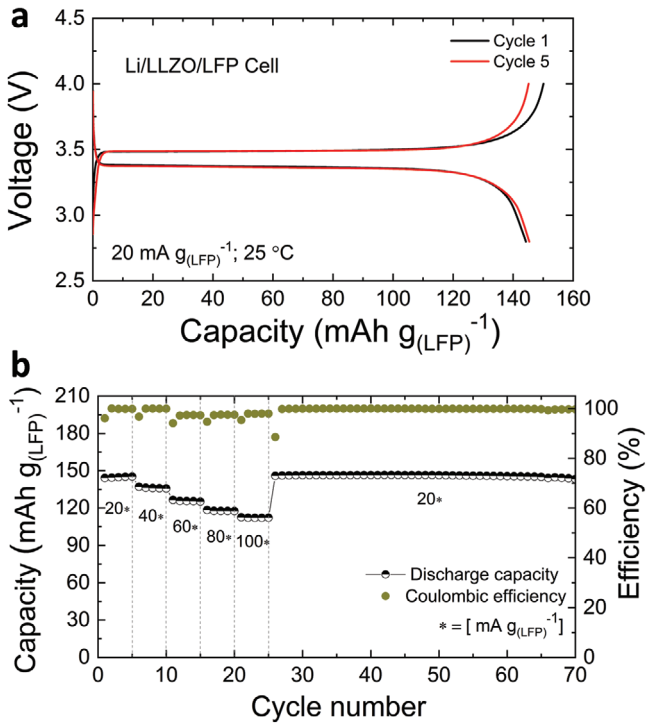

Figure 6. a) Selected charge-discharge profiles of the Li/LLZO/LFP cell with the ILE interlayer at 20 mA $g_{(LFP)}^{-1}$ in a potential window of 2.8–4 V at 25 °C. b) Galvanostatic cycling of the same cell at varying current densities, followed by constant current cycling at 20 mA $g_{(LFP)}^{-1}$.

maintained till the 70th cycle. At higher current densities, good discharge capacities are delivered while maintaining the signature LFP voltage profiles (Figure S10, Supporting Information) that indicates excellent electrochemical stability of the electrolyte.

Unlike the conventional LIBs, a unique feature of SSBs is the assembly of the individual cells in multi-polar stacked configuration, which leads to a higher output voltage and thus a higher volumetric energy density. SE, acting as electrodes' separator as well as medium for ion transport, is a key component in such designs. In the battery pack, the cells are connected in series to add-up the individual cell voltages while ensuring low internal resistances through the reduced terminal connections. As a proof-of-concept, we have expanded the scope of our design by stacking two Li/LLZO/LFP cells in a bipolar configuration (Li/LLZO/LFP-SUS-Li/LLZO/LFP) as shown in **Figure 7**a. A swagelok-type cell was assembled where a stainless steel current collector (SUS) was shared by the adjacent positive (LFP) and negative (Li) electrodes. The open circuit voltage (OCV) for the bipolar cell was measured to be ≈6.1 V (Figure 7a). Figure 7b shows the initial galvanostatic charge/discharge voltage profiles of the bipolar cell at current density of 10 mA $g_{(LFP)}^{-1}$ in the 5.6–8 V voltage window at 25 °C. The signature charge/discharge plateaus associated with the LFP electrode are observed at potentials of 6.9 and 6.8 V, respectively, which are twice the values 3.48 and 3.37 V for the monopolar Li/LLZO/LFP cell. Further, the cell delivers high reversible capacity of ≈145 mAh $g_{(LFP)}^{-1}$ with a coulombic efficiency of > 99%. The capacity values are almost the same as observed for the mono-

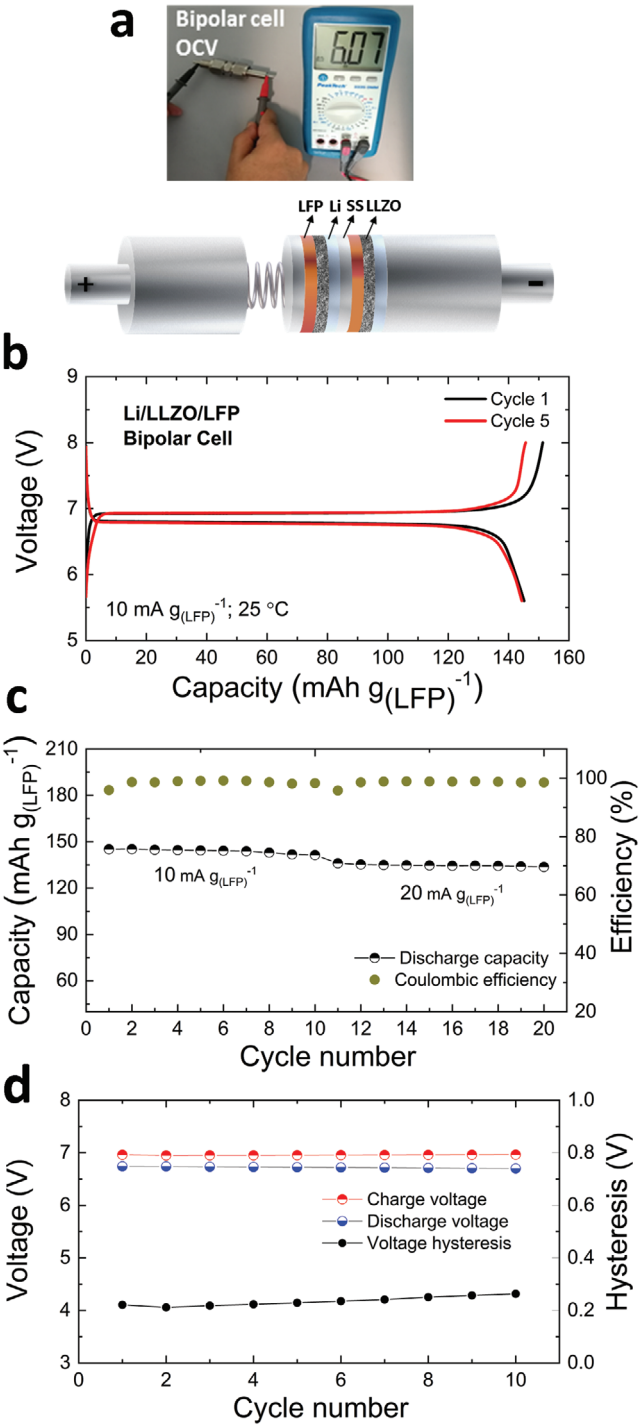

Figure 7. a) Schematic of the Li/LLZO/LFP bipolar cell and measured OCV. b) Selected charge-discharge profiles of the cell at 10 and 20 mA $g_{(LFP)}^{-1}$ in a potential window of 5.6–8 V at 25 °C. c) Galvanostatic cycling and coulombic of the same cell. d) Bipolar cell hysteresis during initial cycles.

polar cell (Figure 6a) suggesting low internal resistance of the cell. Preliminary data for initial 20 cycles at current densities of 10 and 20 mA $g_{(LFP)}^{-1}$ (Figure 7c) indicates that the initial specific capacity is retained quite well. Further the voltage hysteresis, which is the difference of the average charge and discharge

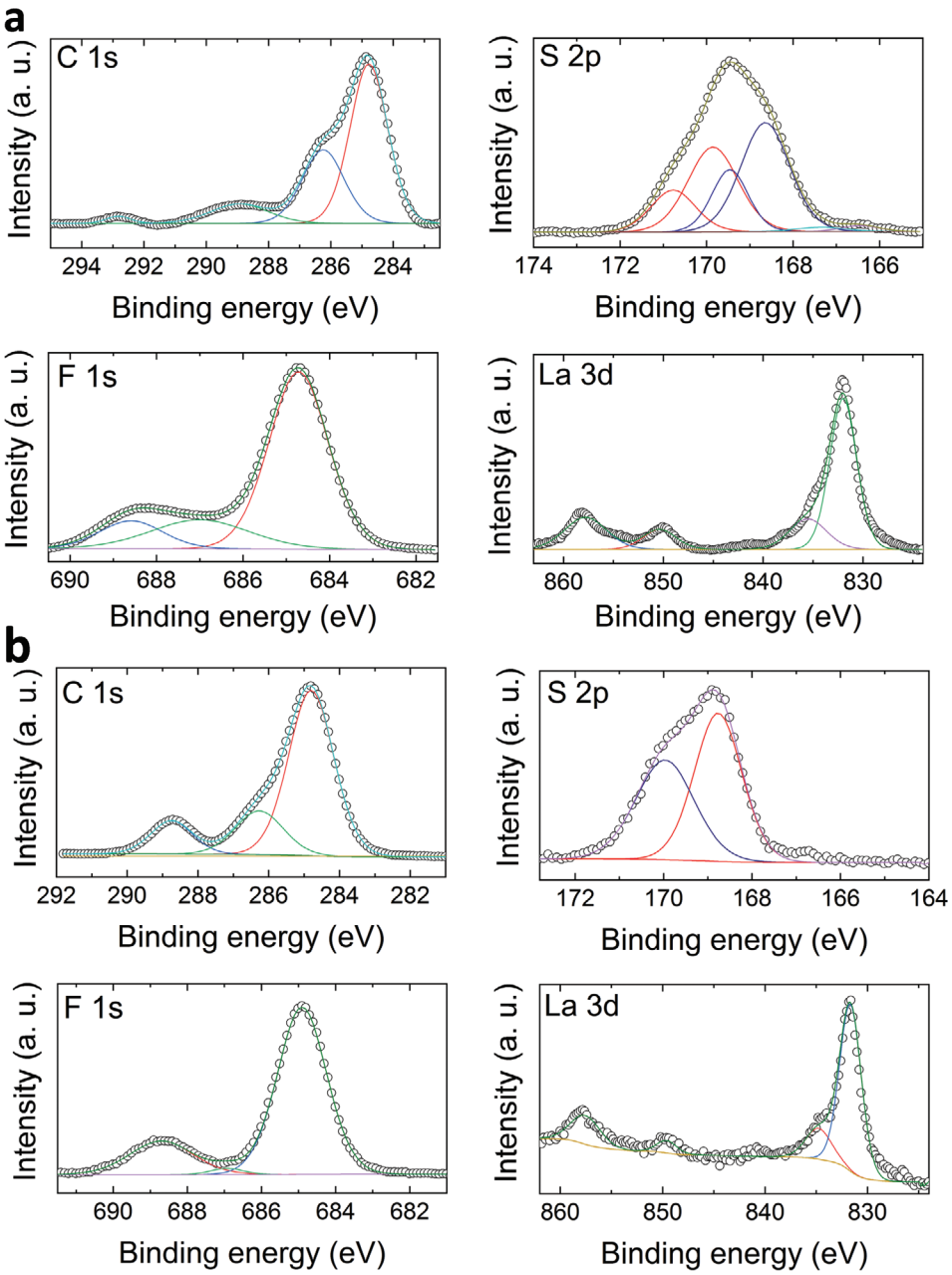

Figure 8. Post-mortem XPS characterization of the cycled LLZO SE surface facing the a) LFP and b) Li electrodes in the Li/LLZO/LFP cell. Details of the experimental data and peak deconvolution in the C1 s, S 2p, F 1s, and La 3d binding energy regions are provided.

voltages, is measured during the initial charge/discharge cycles (Figure 7d). A small voltage hysteresis of ≈250 mV is observed that suggests good cell kinetics. Overall, the results confirm that the series connected individual cells within the Li/LLZO/LFP bipolar configuration operated successfully without any internal short-circuits. We would like to point out that there are only a few reports on stacked cells configurations, mostly based on polymer solid electrolytes.[44–46] To the best of our knowledge this is the first report on multipolar cell configuration in a ceramic SE based SSB.

In order to elucidate the nature of the electrochemical interphase formed between LLZO and the ILE, X-ray photoelectron Spectroscopy (XPS) analysis of the galvanostatically cycled SE was carried out. The results shown in **Figure 8**a,b refer to both sides of the LLZO SE facing the LFP and Li electrodes. Prior to the measurements, the SE was thoroughly washed with isopropanol and dried under vacuum overnight to remove any residual ILE left on the surface. The binding energies of the main features and their assignment to specific functional groups are listed in **Table 2**.

Table 2. Binding energy and assignment of the deconvoluted XPS peaks detected on the LLZO SE surface facing the LFP and Li electrodes in a cycled Li/LLZO/LFP cell.

Spectra	Binding energy [eV]		Possible functional group
	$LiFePO_4$ side	Li side	
C 1s	284.8	284.8	C—C
	286.2	286.2	C—O—C
	288.9	288.9	O—C=O—CF2
	292.8	—	$-CF_2$
S 2p	166.4	—	$-SO_2CF_3$
	167.3	—	$-SO_2CF_3$
	168.6	168.6	$-SO_2CF_2^+/Li_xSO_y$
	169.4	169.4	$-SO_2CF_2^+/Li_xSO_y$
	169.9	—	Metal sulfate (Li_xSO_y)
	170.8	—	Metal sulfate (Li_xSO_y)
F 1s	684.7	684.7	Metal fluorides (LiF)
	687.0	687.0	Organic fluorine (-CF_2/-CF_3)
	688.6	688.6	Organic fluorine (-CF_2/-CF_3)
N 1s	399.0	399.0	Imide groups
	—	400.1	LiTFSI/Pyr_{14}FSI
	402.4	402.4	LiTFSI/Pyr_{14}FSI
La 3d	832	832	La $3d_{5/2}$
	835.5	835.5	La $3d_{5/2}$
	850.4	850.4	La $3d_{3/2}$
	857.8	857.8	La $3d_{3/2}$

The analysis reveals presence of organic and fluorine-, sulfur- and nitrogen- containing surface layers on the SE at both LFP and Li sides. The deconvolution of the C 1s spectrum results in peaks corresponding to C—C, C—O—C, O—C=O and $-CF_2$ species.[47–50] The S 2p peaks at various binding energies indicate $–SO_2CF_3$, $–SO_2CF_2/Li_xSO_y$, and metal sulfates (e.g., Li_xSO_y) originating from the decomposition of the TFSI and FSI anions.[47,51] The F 1s spectrum suggests the presence of LiF and -CF_2/-CF_3 species once more originating from the decomposition of TFSI and FSI.[50] The deconvolution of the N 1s region spectra (shown in Figure S11, Supporting Information) may correspond to the nitrogen functional groups of TFSI and FSI anions, but also the pyrrolidinium cation.[51] Signals for La originating from the LLZO surface were also detected. The deconvoluted peaks in the La 3d spectrum correspond to the typical La $3d_{5/2}$ and La $3d_{3/2}$ which indicate the formation of $La_2(CO_3)_3$ formation on the surface.[52,53] As a supplement analysis, SEM characterization of the SE surface after cycling was also conducted. As shown in Figure S12, Supporting Information, the LLZO surface appears covered by a layer. The elemental mapping of the cycled LLZO (Figure S13, Supporting Information) confirms the presence of surface layers containing F, N and S compounds. Such layers were also observed in previous works.[54,55] On the other hand, the detection of signals from LLZO elements (La) suggests that the interphase layer is of finite thickness, possibly of a few nanometers. From the XPS investigation, it is evident that few nano-meter thick interphase layers are formed at the LLZO SE surface both at the LFP and Li electrodes sides. The layers on either side contain both organic and inorganic species associated to the decomposition of the ILE components, specifically the Pyr_{14} cation and the FSI and TFSI anions. Further in-depth investigation, however, is required to probe formation and evolution of such interphase layers both at open circuit potentials and under biased conditions.

3. Conclusion

This study demonstrates a strategy to improve the ionic transport at the solid–solid Li/LLZO and LFP/LLZO interfaces employing ionic liquid-based electrolyte (ILE) interlayers. From the chemical point of view LLZO and ILE are reciprocally stable as confirmed by Raman and XRD analysis. However, minor ILE decomposition occurs upon cycling, as confirmed by post-mortem XPS and SEM-EDX analysis, resulting in a rather thin layer coating on the solid electrolyte surfaces both at LFP and Li electrodes. From the electrochemical point of view, the ILE interlayers strongly reduce the resistance of the Li/LLZO and LFP/LLZO interfaces to ≈145 and ≈265 Ω cm^2, respectively, consequently lowers the overpotential from 1.35 to 0.35 V. Also the small interface resistance at the Li anode side helps suppress dendritic growth as is evident from stable stripping/plating voltage profiles at high current density of 0.3 mA cm^{-2}. The Li/LLZO/LFP cell employing the ILE interlayers delivers an excellent electrochemical performance with reversible capacity as high as 145 mAh $g_{(LFP)}^{-1}$ and coulombic efficiency exceeding 99.9%. The rate performance is also impressive considering the rather thick LLZO layer, as the cell delivers discharge capacities of ≈136, 125, 117, and 112 mAh $g_{(LFP)}^{-1}$ at 40, 60, 80, and 100 mA $g_{(LFP)}^{-1}$, respectively. Further, to demonstrate the potential of the electrolytes for high voltage applications, a bipolar stacked cell is successfully operated at a high voltage (≈8 V), delivering specific capacity as high as 145 mAh g^{-1}, with a coulombic efficiency greater than 99%.

4. Experimental Section

Synthesis of LLZO Powders and Pellet Processing: LLZO with nominal composition $Li_{6.5}La_{2.5}Ba_{0.5}ZrNbO_{12}$ was prepared by the solid state reaction method.[22] In a typical synthesis, stoichiometric amounts of La_2O_3 (99.99%, Alfa Aesar, pre-heated at 900 °C for 12 h), $Ba(NO_3)_2$ (99%, Alfa Aesar), ZrO_2 (99%, Alfa Aesar), Nb_2O_5 (99.5%, Alfa Aesar), and $LiNO_3$ (99%, Alfa Aesar, 10 wt% extra to make up for the Li loss during high temperature sintering), were properly milled in 2-propanol with planetary ball mill (Pulverisette, Fritsch, Germany) at 200 rpm for 6 h. The metal salts were decomposed by heating the powder mixture at 700 °C for 6 h in air. The obtained powder was ball-milled again to ensure homogenous mixing and then uniaxially pressed into pellets using a hydraulic press (Atlas manual hydraulic press, Specac, UK). To prevent Li loss during high temperature sintering, the pellets were covered with mother powder, initially sintered at 900 °C for 24 h and then at 1100 °C for 3 h. To get desired dimensions, the pellets were polished with Si-carbide sand paper (grit size 400) under argon environment to obtain a thickness of ≈500 µm and a geometric area of ≈0.785 cm^2 for each side.

Synthesis of the Ionic Liquid Electrolyte: The IL, *N*-butyl-*N*-methylpyrrolidinium bis(fluorosulfonyl)imide, Pyr_{14}FSI, was prepared

based on a simple and an environment friendly synthesis route.[28] 0.2 mol of LiTFSI (3M, battery grade) and 0.8 mol of the IL were mixed to form the ILE under argon environment (O_2 < 0.1 ppm and H_2O < 0.1 ppm). The molar fractions of LiTFSI and $Pyr_{14}FSI$ were adjusted to ensure a balance between the number of active charge carriers (Li ions) and viscosity of the IL. The ILE was further dried at 60 °C under vacuum to decrease the water content below 5 ppm, as detected by Karl–Fischer measurements.

Preparation of LFP Positive Electrodes (Cathodes): Carbon-coated LFP was synthesized via a solid state method.[56] Stoichiometric amounts of lithium carbonate (Li_2CO_3; Aldrich, 99.95%), ammonium hydrogen phosphate ($(NH_4)_2HPO_4$; Merck, > 99%), and iron oxalate (FeC_2O_4; ACROS ORGANICS, > 99%) were used as starting materials. The powders were mixed by means of high-energy ball milling for 3 h at a speed of 400 rpm (powder to ball ratio is 1:10). The recovered mixture was ground thoroughly and pre-heated at 320 °C for 10h (3 K min^{-1}) followed by calcination at 500 °C for 6 h under nitrogen atmosphere. The obtained LFP powder was dispersed in an aqueous solution of sucrose (LFP:sucrose 2:1) for 2 h at 400 rpm using a planetary ball mill. After removing the solvent the powder was thoroughly ground and once more fired at 700 °C for 2 h under argon atmosphere to obtain carbon-coated LFP.[57] By means of elemental analysis, the carbon content was determined to be 0.5 wt% with respect to LFP.

Material Characterization: The crystal structure analysis of LLZO was carried out by X-ray diffractometry (Cu Kα, 40 kV, 40 mA Bruker D8). For SEM and energy-dispersive X-ray spectroscopy (EDS), a LEO GEMINI 1550 VP instrument equipped with a silicon drift detector (OXFORD Instruments) was used. Raman spectroscopy was carried out at room temperature (≈25 °C) with a confocal Raman microscope (InVia, RENISHAW) in the spectral range 50–1300 cm^{-1} using a 532 nm HeNe laser excitation source. Every spectrum recorded resulted from the average of 3 acquisitions of 5 s each. For the mapping of the sample surface and in-depth, the Volume (Stream HR) acquisition mode was used. The data were analyzed using inVia WiRE 4.4 Software. XPS measurements were carried out at the LLZO surface to determine the elemental composition and for depth profiling of the sample surfaces. The analysis was carried out at the cathode (LFP) side. Prior to the measurements, the LFP cathode was detached and the surface of LLZO SE was thoroughly washed with isopropanol and then dried overnight under vacuum. The measurements were done using monochromatized Al Kα (1486.6 eV) radiation source with a detection angle of 45°, using pass energies at the analyzer of 93.9 and 29.35 eV for survey and detail spectra, respectively. For binding energy calibration, the main C (1s) peak was set to 284.8 eV.

Cell Fabrication and Electrochemical Tests: LLZO pellets were sputtered (LEICA EM ACE600) with gold on both sides to form contacts, which acted as Li quasi-blocking electrodes. For Li symmetric cells fabrication, LLZO pellets were sandwiched between two Li metal discs (Sigma Aldrich) in argon-filled glove-box (H_2O and O_2 < 1 ppm) with and without the interposition of the ILE-interlayers at the interfaces. Cells without ILE were heated till 180 °C (melting temperature of Li) to promote Li-SE mutual contact. For cells based only on ILE, stainless steels are used as current collectors and glass fiber membranes as separators. Both Li-blocking and reversible cells were assembled in swagelok-type cell holders. EIS was carried out in the range of 6 MHz to 100 mHz with a sinus amplitude of 10 mV using a frequency response analyzer (ZAHNER-Elektrik GmbH). A Bio-Logic VMP-3 potentiostat was used to conduct the Li stripping/plating tests at current densities ranging from 0.05 to 0.3 $mAcm^{-2}$. Complete cells were assembled either in monopolar or bipolar configurations in swagelok-type cells. In bipolar cells a stainless steel current collector (SUS) was shared by the adjacent positive (LFP) and negative (Li) electrodes. A single cell comprised of a polished LLZO pellet sandwiched between the LFP positive electrode and the lithium metal negative electrode. The positive electrode composition was 85 wt% LFP, 10 wt% conductive carbon (C-ENERGY Super C65, IMERYS) and 5 wt% binder (polyvinylidene difluoride, PVdF, Solef 6020, Solvay) using a 4.0 wt% solution of PVdF in *N*-methyl-2-pyrrolidon (NMP; anhydrous, >99.5%; Sigma-Aldrich). The resulting slurry was homogenized by planetary ball milling for 2 h. The obtained slurry was cast on aluminum foil, serving as current collector (thickness: 20 µm; battery grade), utilizing a laboratory doctor blade (wet film thickness of 200 µm). After immediate pre-drying in an atmospheric oven (ED-115, Binder) at 60 °C for 2h, the resulting electrode tapes were stored at room temperature in the dry room overnight. Disc electrodes were punched (geometric area: 1.13 cm^2) and pressed at 10 tons for 10 s (Atlas manual hydraulic press, Specac, UK) also carried out under dry atmosphere. Finally, after drying for 16 h at 120 °C under dynamic vacuum the electrodes had an average active material loading of 2.5 mg cm^{-2}. The porosity of LFP cathodes was filled with a controlled amount of ILE (~ 2 µL). At the Li/LLZO interface less than 1 µL of ILE was used to wet the SE on the negative electrode side. Galvanostatic cycling tests were carried out in the voltage range from 2.8 to 4.0 V for monopolar and 5.6 to 8 V for bipolar cells at various current densities (10–100 mA g^{-1}) using Arbin electrochemical workstation. The temperature during testing was kept at 25 °C. The cyclic voltammetry (CV) test was carried out at a linear scan rate of 0.1 mV s^{-1} in a potential range 2.6–4.2 V at 25 °C.

Supporting Information

Supporting Information is available from the Wiley Online Library or from the author.

Acknowledgements

All authors acknowledge the Helmholtz Association for the basic funding. S.A.P. acknowledges the grant from the Alexander-von-Humboldt Foundation. G.-T.K., M.K., M.H., and S.P. acknowledge support of the German Federal Ministry of Education and Research (BMBF) within the FestBatt (03XP0175B), Hi-Safe (03XP0138A-C), and LILLINT (03XP0225D) projects. This work contributes to the research performed at CELEST (Center for Electrochemical Energy Storage Ulm-Karlsruhe).

Conflict of Interest

The authors declare no conflict of interest.

Keywords

bipolar cells, interfacial modifications, ionic liquids, Li dendrites, Li garnet, solid-electrolytes, solid-state batteries

Received: January 14, 2020
Published online:

[1] A. Armstrong, P. Bruce, *Nature* **1996**, *381*, 499.
[2] J. Tarascon, M. Armand, *Nature* **2001**, *414*, 359.
[3] J. B. Goodenough, Y. Kim, *Chem. Mater.* **2010**, *22*, 587.
[4] V. Thangadurai, S. Narayanan, D. Pinzaru, *Chem. Soc. Rev.* **2014**, *43*, 4714.
[5] P. Knauth, *Solid State Ionics.* **2009**, *180*, 911.
[6] Y. Kato, S. Hori, T. Saito, K. Suzuki, M. Hirayama, A. Mitsui, M. Yonemura, H. Iba, R. Kanno, *Nat. Energy* **2016**, *1*, 16030.
[7] P. R. Chinnam, S. L. Wunder, *J. Mater. Chem. A* **2013**, *1*, 1731.
[8] K. Xu, *Chem. Rev.* **2004**, *104*, 4303.

[9] G. Zhou, F. Li, H.-M. Cheng, *Energy Environ. Sci.* **2014**, *7*, 1307.
[10] Y. Zhu, X. He, Y. Mo, *ACS Appl. Mater. Interfaces* **2015**, *7*, 23685.
[11] L. J. Miara, W. D. Richards, Y. E. Wang, G. Ceder, *Chem. Mater.* **2015**, *27*, 4040.
[12] X. Han, Y. Gong, K. Fu, X. He, G. T. Hitz, J. Dai, A. Pearse, B. Liu, H. Wang, G. Rubloff, Y. Mo, V. Thangadurai, E. D. Wachsman, L. Hu, *Nat. Mater.* **2016**, *16*, 572.
[13] C.-L Tsai, V. Roddatis, C. V. Chandran, Q. Ma, S. Uhlenbruck, M. Bram, P. Heitjans, O. Guillon, *ACS Appl. Mater. Interfaces* **2016**, *8*, 10617.
[14] B. Wu, S. Wang, J. Lochala, D. Desrochers, B. Liu, W. Zhang, J. Yang, J. Xiao, *Energy Environ. Sci.* **2018**, *11*, 1803.
[15] K. Fu, Y. Gong, B. Liu, Y. Zhu, S. Xu, Y. Yao, W. Luo, C. Wang, S. D. Lacey, J. Dai, Y. Chen, Y. Mo, E. Wachsman, L. Hu, *Sci. Adv.* **2017**, *3*, e1601659.
[16] W. Luo, Y. Gong, Y. Zhu, Y. Li, Y. Yao, Y. Zhang, K. Fu, G. Pastel, C.-F. Lin, Y. Mo, E. Wachsman, L. Hu, *Adv. Mater.* **2017**, *29*, 1606042.
[17] C. Wang, Y. Gong, B. Liu, K. Fu, Y. Yao, E. Hitz, Y. Li, J. Dai, S. Xu, W. Luo, E. D. Wachsman, L. Hu, *Nano Lett.* **2017**, *17*, 565.
[18] K. Fu, Y. Gong, G. T. Hitz, D. W. McOwen, Y. Li, S. Xu, Y. Wen, L. Zhang, C. Wang, G. Pastel, J. Dai, B. Liu, H. Xie, Y. Yao, E. D. Wachsman, L. Hu, *Energy Environ. Sci.* **2017**, *10*, 1568.
[19] S. Ohta, T. Kobayashi, J. Seki, T. Asaoka, *J. Power Sources* **2012**, *202*, 332.
[20] B. Liu, K. Fu, Y. Gong, C. Yang, Y. Yao, Y. Wang, C. Wang, Y. Kuang, G. Pastel, H. Xie, D. Wachsman, L. Hu, *Nano Lett.* **2017**, *17*, 4917.
[21] W. Zhou, S. Wang, Y. Li, S. Xin, A. Manthiram, J. B. Goodenough, *J. Am. Chem. Soc.* **2016**, *138*, 9385.
[22] S. A. Pervez, P. Ganjeh-Anzabi, U. Farooq, M. Trifkovic, E. P. L. Roberts, V. Thangadurai, *Adv. Mater. Interfaces* **2019**, *6*, 1900186.
[23] B. Liu, Y. Gong, K. Fu, X. Han, Y. Yao, G. Pastel, C. Yang, H. Xie, E. D. Wachsman, L. Hu, *ACS Appl. Mater. Interfaces* **2017**, *9*, 18809.
[24] N. Li, Z. Weng, Y. Wang, F. Li, H.-M. Cheng, H. Zhou, *Energy Environ. Sci.* **2014**, *7*, 3307.
[25] L. Wang, Y. Wang, Y. Xia, *Energy Environ. Sci.* **2015**, *8*, 1551.
[26] D. R. MacFarlane, M. Forsyth, P. C. Howlett, M. Kar, S. Passerini, J. M. Pringle, H. Ohno, M. Watanabe, F. Yan, W. Zheng, S. Zhang, J. Zhang, *Nat. Rev. Mater.* **2016**, *1*, 15005.
[27] M. Montanino, F. Alessandrini, S. Passerini, G. B. Appetecchi, *Electrochim. Acta* **2013**, *96*, 124.
[28] G. A. Elia, U. Ulissi, S. Jeong, S. Passerini, J. Hassoun, *Energy Environ. Sci.* **2016**, *9*, 3210.
[29] S. Ohta, T. Kobayashi, T. Asaoka, *J. Power Sources* **2011**, *196*, 3345.
[30] V. Thangadurai, W. Weppner, *J. Am. Ceram. Soc.* **2005**, *88*, 411.
[31] F. Shen, M. B. Dixit, X. Xiao, K. B. Hatzell, *ACS Energy Lett.* **2018**, *3*, 1056.
[32] C. A. Geiger, E. Alekseev, B. Lazic, M. Fisch, T. Armbruster, R. Langner, M. Fechtelkord, N. Kim, T. Pettke, W. Weppner, *Inorg. Chem.* **2011**, *50*, 1089.
[33] M. Kotobuki, K. Kanamura, Y. Sato, T. Yoshida, *J. Power Sources* **2011**, *196*, 7750.
[34] E. J. Cussen, *Chem. Commun.* **2006**, 412.
[35] J. T. S. Irvine, D. C. Sinclair, A. R. West, *Adv. Mater.* **1990**, *2*, 132.
[36] G. Larraz, A. Orera, A. Sanjuan, *J. Mater. Chem. A* **2013**, *1*, 11419.
[37] T. Thompson, J. Wolfenstein, J. L. Allen, M. Johannes, A Huq, I. N. David, J. Sakamoto, *J. Mater. Chem. A* **2014**, *2*, 13431.
[38] A. Sharafi, S. Yu, M. Naguib, M. Lee, C. Ma, H. M. Meyer, J. Nanda, M. Chi, D. J. Siegel, J. Sakamoto, *J. Mater. Chem. A* **2017**, *5*, 13475.
[39] K. Yan, H.-W. Lee, T. Gao, G. Zheng, H. Yao, H. Wang, Z. Lu, Y. Zhou, Z. Liang, Z. Liu, S. Chu, Y. Cui, *Nano Lett.* **2014**, *14*, 6016.
[40] G. Zheng, S. W. Lee, Z. Liang, H.-W. Lee, K. Yan, H. Yao, H. Wang, W. Li, S. Chu, Y. Cui, *Nat. Nanotechnol.* **2014**, *9*, 618.
[41] B. Xu, W. Li, H. Duan, H. Wang, Y. Guo, H. Li, H. Liu, *J. Power Sources* **2017**, *354*, 68.
[42] A. K. Padhi, K. S. Nanjundaswamy, J. B. Goodenough, *J. Electrochem. Soc.* **1997**, *144*, 1188.
[43] C. Masquelier, L. Croguennec, *Chem. Rev.* **2013**, *113*, 6552.
[44] S. H. Kim, K. H. Choi, S. J. Cho, J. T. Yoo, S. S. Lee, S. Y. Lee, *Energy Environ. Sci.* **2018**, *11*, 321.
[45] G. B. Appetecchi, J. H. Shin, F. Alessandrini, S. Passerini, *J. Power Sources* **2005**, *143*, 236.
[46] T. Sato, T. Morinaga, S. Marukane, T. Narutomi, T. Igarashi, Y. Kawano, K. J. Ohno, T. Fukuda, Y. Tsujii, *Adv. Mater.* **2011**, *23*, 4868.
[47] A. Schechter, D. Aurbach, H. Cohen, *Langmuir* **1999**, *15*, 3334.
[48] D. Aurbach, E. Pollak, R. Elazari, G. Salitra, C. S. Kelley, J. Affinito, *J. Electrochem. Soc.* **2009**, *156*, A694.
[49] S. Xiong, K. Xie, Y. Diao, X. Hong, *J. Power Sources* **2013**, *236*, 181.
[50] R. Dedryvere, S. Leroy, H. Martinez, F. Blanchard, D. Lemordant, D. Gonbeau, *J. Phys. Chem. B* **2006**, *110*, 12986.
[51] a) G. G. Eshetu, T. Diemant, S. Grugeon, J. Behm, R. S. Laruelle, M. Armand, S. Passerini, *ACS Appl. Mater. Interfaces* **2016**, *8*, 16087; b) J. Ingram, L. A. Curtiss, J. W. Freeland, *Adv. Energy Mater.* **2019**, *9*, 1803440.
[52] J. F. Moulder, W. F. Stickle, P. E. Sobol, K. D. Bomben, *Handbook of X-ray Photoelectron Spectroscopy: A Reference Book of Standard Spectra for Identification and Interpretation of XPS Data*, Physical Electronics Division, Perkin-Elmer Corporation, **1992**.
[53] M. Zarabian, M. Bartolini, P. Pereira-Almao, V. Thangadurai, *J. Electrochem. Soc.* **2017**, *164*, A1133.
[54] M. R. Busche, T. Drossel, T. Leichtweiss, D. A. Weber, M. Falk, M. Schneider, M.-L. Reich, H. Sommer, P. Adelhelm, J. Janek, *Nat. Chem.* **2016**, *8*, 426.
[55] K. Fu, Y. Gong, S. Xu, Y. Zhu, Y. Li, J. Dai, C. Wang, B. Liu, G. Pastel, H. Xie, Y. Yao, Y. Mo, E. Wachsman, L. Hu, *Chem. Mater.* **2017**, *29*, 8037.
[56] A. Yamada, S. C. Chung, K. J. Hinokuma, *J. Electrochem. Soc.* **2001**, *148*, A224.
[57] N. Laszczynski, A. Birrozzi, K. Maranski, M. Copley, M. E. Schuster, S. Passerini, *J. Mater. Chem. A* **2016**, *4*, 17121.